PCCP

ROYAL SOCIETY OF CHEMISTRY

PAPER

View Article Online
View Journal | View Issue

Cite this: *Phys. Chem. Chem. Phys.*, 2023, **25**, 3144

Unveiling the correlation between structural and magnetic ordering in nano $Co_{1-x}Ni_xTeO_4$†

Akhilesh Kumar Patel, [a] S. Shanmukharao Samatham, [b] Ekta Rani, [c] K. G. Suresh[a] and Harishchandra Singh *[ac]

Nanomaterials with unique structures and exotic magnetic phenomena are always intriguing; however, the direct correlation of structural and magnetic ordering up to a few nanometers remains critical. We report structural and magnetic properties of sol–gel grown $Co_{1-x}Ni_xTeO_4$ (x = 0, 0.5 and 1) nanoparticles. An increase in the calcination temperature leads to the enhancement of the particle size and structural ordering. This is accompanied by changes in the magnetic interactions as well. Calcination at lower temperatures retains the short-range non-crystalline structure and superparamagnetic behavior, while calcination at higher temperatures results in long-range ordering in both the crystal and magnetic structures. Superparamagnetic to antiferromagnetic ordering observed from temperature- and field-dependent magnetization is attributed to the changes in structural ordering. This study presents a new family of nanomaterials displaying stable magnetic order up to ~6 nm, where the magnetic properties can be uniquely controlled by changing the structural ordering.

Received 30th November 2022,
Accepted 15th December 2022

DOI: 10.1039/d2cp05592a

rsc.li/pccp

Introduction

Technological advances for subsequent generation devices have escalated the research at the nanoscale as an unprecedented change in nanostructures' structural, electronic, and vibration properties has been evidenced due to the quantum confinement effect and/or increase in surface to volume ratio.[1–3] Depending on their properties, such nanostructures have been found to be suitable for different applications.[2,4] Interest in magnetic nanostructures has been boosted in the past few decades by virtue of their potential in diverse fields, such as ultrahigh-density recording,[5] medical diagnostics,[6] catalysis,[7] and sensors.[8] Apart from the properties mentioned above, the magnetic behavior of the nanostructures also differs from that of their bulk counterparts. This is because size reduction to a nanometric scale strongly rearranges the magnetic moment/domain. Thus, exploring magnetic materials of varying sizes is essential and can reveal novel promising applications.

The manifestation of magnetic properties in nanostructures has been reported for several systems, such as $GdAl_2$,[9] $Ni(OH)_2$,[10] $La_{1-x}Sr_xCoO_3$,[11] and perovskite manganite $R_{1-x}A_xMnO_3$ (R = La, Pr, Sm *etc.*, and A = Ca, Sr, Ba, and Pb).[12,13] For example, $GdAl_2$ nanocrystallites displayed broadening in the ferromagnetic (FM) transition, rather than shift, with a decrease in nanocrystallite size along with superparamagnetic behavior for smaller nanocrystallites (~18 nm) below 30 K.[9] $Ni(OH)_2$ nanoparticles of average size ~8 nm, on the other hand, displayed paramagnetic behavior at higher temperatures and a paramagnet to ferromagnet transition with a decrease in temperature.[10] Moreover, for one of the most studied and applied compounds, Fe_2O_3, both coercivity and remanence were found to approach zero at a particle size of ~19.3 nm.[3] Though the size-dependent magnetic interaction has already been investigated, a direct correlation among particle size, crystallographic structural ordering, and magnetic properties is lacking.

Recently, nanostructured transition metal tellurates/tellurides have come into the limelight as potential candidates for energy applications.[14,15] Moreover, cobalt-based tellurates/tellurides display intriguing magnetic behavior, such that $CoTeO_4$,[14] CoTe,[16] $Co_2Te_3O_8$,[17] and Co_3TeO_6[18,19] either show weak FM or antiferromagnetic (AFM) transition in polycrystalline form. However, the effect of calcination temperature on the crystallization and the particle size-dependent magnetic properties of telluride nanoparticles has not yet been studied. Therefore, from the application point of view, it is interesting to take up a system, such as $CoTeO_4$, and study the effects of substitutions and preparation conditions, such as calcination temperature, on the particle size and magnetic field properties. In the present work, sol–gel-grown $Co_{1-x}Ni_xTeO_4$ (x = 0, 0.5, and 1) nanoparticles with different sizes are studied to

[a] *Department of Physics, Indian Institute of Technology Bombay, Mumbai 400 076, India*
[b] *Department of Physics, Chaitanya Bharathi Institute of Technology, Gandipet, Hyderabad 500 075, India*
[c] *Nano and Molecular Systems Research Unit, University of Oulu, FIN-90014, Finland. E-mail: Harishchandra.Singh@oulu.fi*

† Electronic supplementary information (ESI) available. See DOI: https://doi.org/10.1039/d2cp05592a

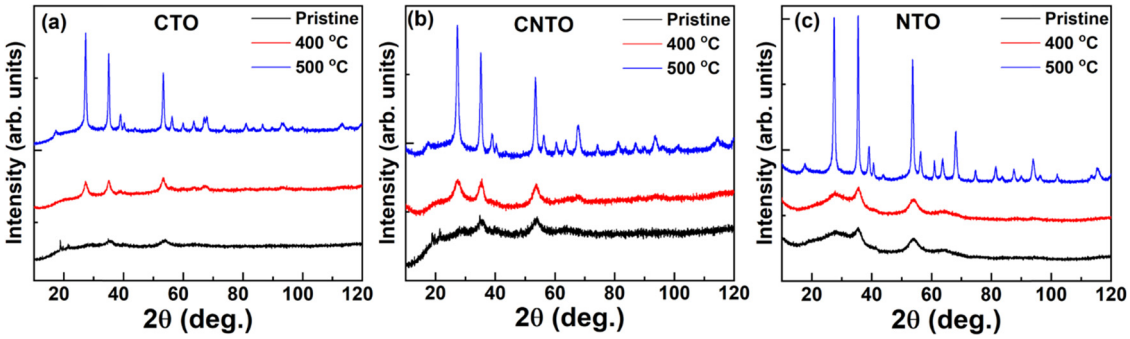

Fig. 1 The room temperature X-ray diffraction patterns of pristine and calcined (a) CTO, (b) CNTO, and (c) NTO showing increases in the crystallinity as the calcination temperature is increased.

investigate their structural and magnetic properties. Following detailed microstructural and structural analysis, the correlation of structural ordering and magnetic interactions is explored with varying calcination temperatures.

Experimental

Synthesis

$Co_{1-x}Ni_xTeO_4$ (x = 0, 0.5 and 1) compounds were prepared by a sol–gel method using the initial compounds of $Co(NO_3)_2{\cdot}6H_2O$, $Ni(NO_3)_2{\cdot}6H_2O$, and $H_2O_4Te{\cdot}2H_2O$. The constituent compounds were taken and mixed in distilled water using a magnetic stirrer for 3 h. Post stirring, each solution was dried on a hot plate at 80 °C. The dried powder of each composition was divided into three parts and kept for calcination at different temperatures for different durations (Table S1, ESI†). Hereafter, $CoTeO_4$, $Co_{0.5}Ni_{0.5}TeO_4$, and $NiTeO_4$, (MTO; M = Co, Co/Ni, and Ni), are referred to as CTO, CNTO, and NTO, respectively.

Instrumentation

The room-temperature X-ray diffraction (XRD) patterns were recorded on well-ground specimens using a PANalytical X-ray diffractometer. The scanning electron microscopy (SEM) and energy dispersive spectroscopy (EDS) data were collected using a Field Emission Gun FEG-SEM (JEOL JSM-7600F FEG-SEM). Transmission electron microscopy (TEM) measurements were carried out using a JEOL JEM2200FS EFTEM/STEM instrument. Selected area electron diffraction (SAED) was performed by FEG-TEM. Magnetic moments *versus* temperature and magnetic field were measured using a SQUID vibrating sample magnetometer (VSM). The magnetic measurements were carried out in zero-field cooling (ZFC) and field-cooling warming

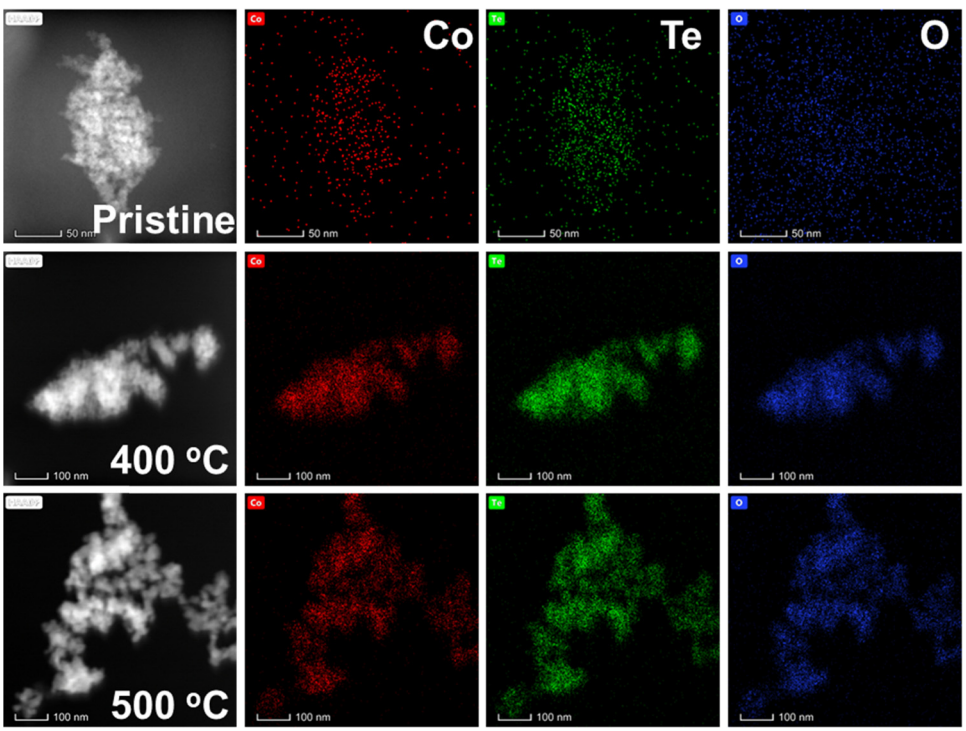

Fig. 2 The TEM-EDS mapping of pristine and calcined (400 °C and 500 °C) CTO.

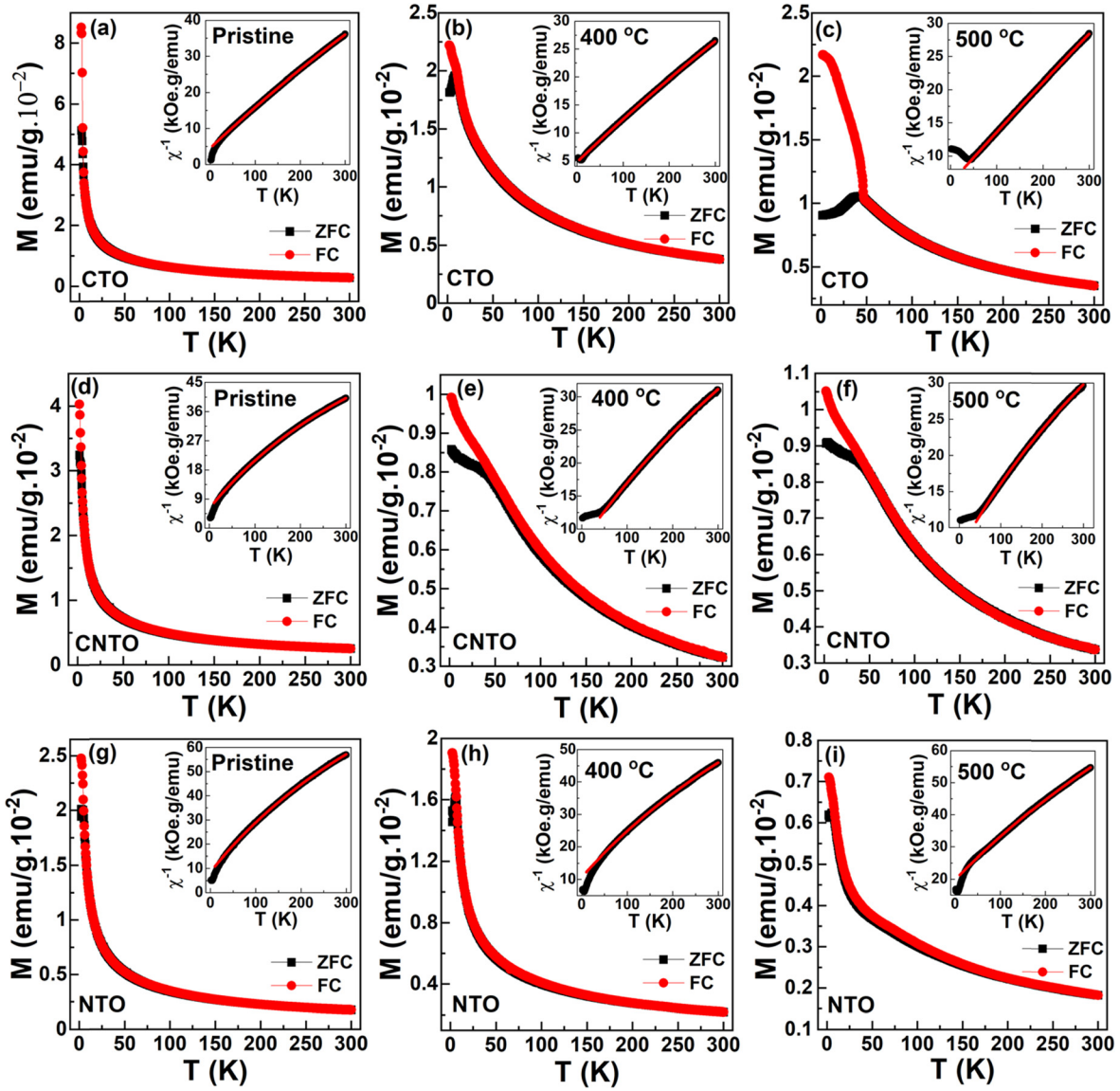

Fig. 3 (a) Temperature-dependent magnetization at 100 Oe for (a–c) CTO, (d–f) CNTO and (g–i) NTO for pristine and calcined (400 °C and 500 °C) compounds along with the corresponding modified Curie–Weiss fitting at 100 Oe ZFC (insets).

(FCW) processes. In the ZFC process, the specimen was cooled down to 2 K (from 300 K) in the absence of a magnetic field and then a field was applied. The data were collected during warming. In the FCW process, the specimen was cooled in the presence of a magnetic field and the data were collected during warming without switching off the applied magnetic field.

Results and discussion

The room temperature XRD patterns of the pristine (as-prepared) MTO and those calcined at 400 and 500 °C are shown in Fig. 1(a–c). The non-crystalline nature of the pristine and low-temperature calcined (400 °C) MTOs is evident from the broad peaks of the patterns. However, crystallinity is found to enhance as the temperature is increased to 500 °C. This observation corroborates a recent study, wherein a single crystalline phase is obtained at a calcination temperature of 600 °C.[14] Thus, the transformation of short-range structural ordering (*i.e.*, non-crystalline structure) to long-range structural ordering (crystalline structure) is observed with the increase in calcination temperature. EDS spectra of each compound at different calcination temperatures (Fig. S1(a–i), ESI†) and corresponding atomic percentages (Table S2, ESI†) suggest the elemental homogeneity of the grown nanomaterials.[20] Fig. S2(a–i) (ESI†) shows the high-resolution SEM images for pristine $Co_{1-x}Ni_xTeO_4$ (x = 0, 0.5 and 1) compounds along with their calcined counterparts. The morphology of these nanostructures is found to be spherical in nature. An increase in nanoparticle size and its crystallinity with the increase in calcination temperature is evident. Moreover, the SEM images of the pristine compounds (Fig. S2(a, d and g), ESI†) show that

nanoparticles are not well separated, whereas these nanoparticles start to separate with the calcination temperature (Fig. S2(c, f and i), ESI†). The TEM-EDS mapping (Fig. 2) for pristine and calcined CTO nanoparticles further shows the homogeneous distribution of Co, Te, and O elements. The calculated elemental atomic percentages also follow the elemental atomic percentages as found from SEM-EDS. The particle sizes of the CTO compounds, as inferred from TEM (Fig. S3, ESI†), show an average size of ~3 nm for the pristine compound, whereas an increase in average size from ~10 to ~25 nm with the increase in the calcination temperature from 400 °C to 500 °C is noted. The average particle sizes for all compounds are given in Table S3 (ESI†).

The magnetization as a function of temperature (M–T) in 100 Oe is measured for the pristine nanoparticles and their calcined counterparts. M–T plots of CTO are shown in Fig. 3(a–c). Fig. 3(a) shows magnetization behavior of the pristine compound, wherein no signatures of magnetic ordering are found down to 5 K. To estimate the possible existing magnetic correlations, the inverse susceptibility of the same is fitted using the Curie–Weiss law,

$$\chi = \chi_0 + C/(T - \theta_{CW}) \quad (1)$$

where χ_0 is the independent magnetic susceptibility, C is the Curie constant, and θ_{CW} is the Curie–Weiss temperature. The fit is shown in the inset of Fig. 3(a). The fit resulted in a paramagnetic Curie–Weiss temperature of −37.6 K and an effective magnetic moment of $4.1\mu_B$. Although the pristine compound does not seem to order magnetically down to 5 K, a negative θ_{CW} (= −37.6 K) signifies AFM correlations of the spins. Despite magnetic correlations, the magnetic order might be prevented by the lack of atomic ordering in their respective atomic/Wyckoff positions due to the non-crystalline nature of the pristine compound. As the calcination temperature increases, the negative θ_{CW} is found to increase from −36.7 K (pristine) to −58.4 K (for 400 °C). An increase in negative θ_{CW} is understood to correlate with the crystallinity enhancement at elevated calcination temperatures. This indicates that the magnetic ordering is stabilized with the increase in crystallinity. The compound calcined at 400 °C (Fig. 3(b)) exhibits a sharp peak at 8.9 K, at which the bifurcation of ZFC and FCW also onsets. Inferring from the negative paramagnetic Curie–Weiss temperature, the observed transition results from the AFM behavior with a Néel temperature of T_N = 8.9 K. A further increase in calcination temperature has led to an enhanced T_N from 8.9 K (400 °C) to 43.5 K (500 °C). Such an enhancement is supported by the increased θ_{CW}, indicating strong AFM interactions in the nanoparticles. For CNTO, the pristine compound exhibits a negative θ_{CW} but does not order magnetically down to 5 K (Fig. 3(d)). However, it exhibits AFM order below 39.1 K when calcined at 400 °C (Fig. 3(e)) and 42.7 K when calcined at 500 °C (Fig. 3(f)). Similarly, the pristine NTO does not order magnetically down to 5 K (Fig. 3(g)), whereas for calcined specimens, T_N is found to be 5.5 K (400 °C: Fig. 3(h)) and 6.1 K (500 °C: Fig. 3(i)). The particulars of the calcination temperatures, T_N and θ_{CW}, and the effective magnetic moments are detailed in Table 1. The observed variation in the effective magnetic moments of each CTO compound could be related to the crystalline nature of these compounds.

Table 1 Magnetic transition temperature (T_N), Curie–Weiss temperature (θ_{CW}), and effective magnetic moments (μ_{eff}) of CTO, CNTO and NTO compounds at different calcination temperatures

Calcination temperature	T_N (K)	θ_{CW} (K)	μ_{eff} (μ_B f.u.$^{-1}$)
CTO			
Pristine	—	−37.6 ± 0.1	4.13 ± 0.01
400 °C	8.9	−58.4 ± 0.1	4.91 ± 0.01
500 °C	43.5	−74.1 ± 0.2	5.02 ± 0.01
CNTO			
Pristine	—	−32.5 ± 0.1	3.21 ± 0.01
400 °C	39.1	−55.3 ± 0.5	4.24 ± 0.02
500 °C	42.7	−61.8 ± 0.6	4.02 ± 0.02
NTO			
Pristine	—	−34.4 ± 0.2	2.84 ± 0.01
400 °C	5.5	−62.7 ± 0.5	3.32 ± 0.02
500 °C	6.1	−125.2 ± 0.7	3.41 ± 0.02

Fig. 4 shows the isothermal magnetization *versus* magnetic fields (M–H) measured at 2, 100, and 300 K. The measurements were carried out in the ZFC process. M–H curves were recorded in five quadrants (0 → 70 → 0 → −70 → 0 → 70 kOe) by sweeping the magnetic field. For the sake of clarity and to be precise, we discuss the first quadrant of M–H data. Fig. 4(a–c) shows the curves for CTO. Pristine CTO exhibits an almost non-linear behavior with a non-saturating magnetic moment of about 12.5 emu g^{-1} under the influence of 70 kOe. However, in the paramagnetic state, *i.e.*, at 100 and 300 K, the M–H curves are linear. Though the 2 K isotherm is still non-linear for a 400 °C calcined CTO, it is linear for a 500 °C calcined compound indicating the AFM behavior. A quasi-non-linear behavior with excess non-saturating magnetic moment is attributed to the non-crystalline nature of the pristine and 400 °C calcined compounds. A similar nature is observed in the CNTO and NTO compounds, as shown in Fig. 4(d–f) and (g–i), respectively. The M–H data of MTO commonly reveals the stable magnetic order with the improvement of the crystallinity as the calcination temperature is increased.

Fig. 5 shows the schematic diagram of the morphological, structural, and magnetization behavior of MTO with calcination temperature, summarizing the transition of the magnetic interaction from superparamagnetic to AFM because of the change in short-range structural ordering to long-range structural ordering. It is evident that the pristine nanoparticles are non-crystalline in nature, while the calcination at high temperature induces the long-range crystalline order as indicated by the horizontal arrow in Fig. 5. Under H = 0, these nanoparticles show superparamagnetic behavior and the presence of a magnetic field tries to bring an overall magnetic order by orienting the spins of the individual nanoparticles in the field's direction. As a result, soft FM-like behavior is observed in the magnetization *vs.* magnetic field isotherms of these non-crystalline pristine nanoparticles of MTO. The origin of net magnetic moment in these compounds could be due to the uncompensated Co^{2+}/Ni^{2+} ions at the surface

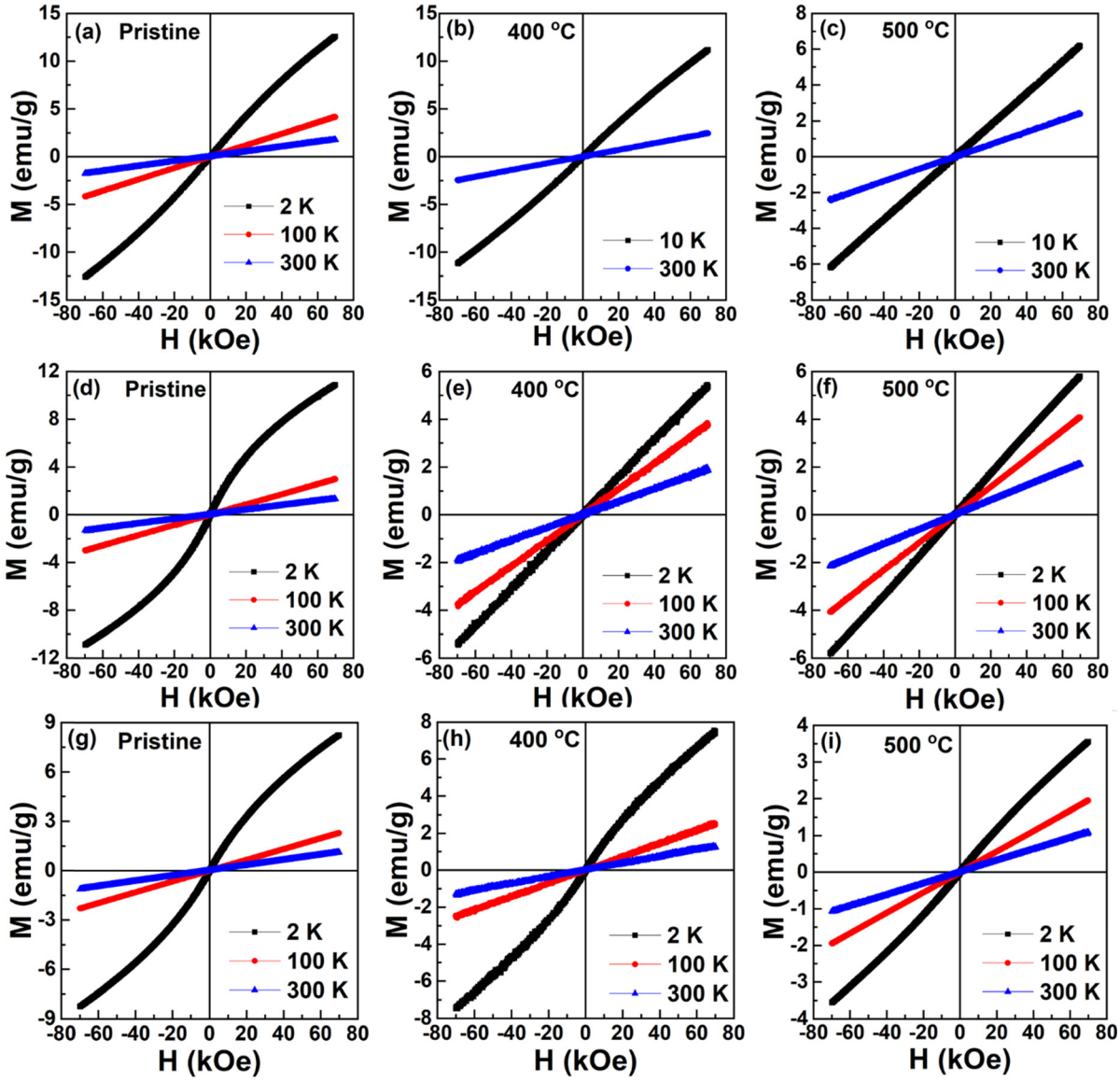

Fig. 4 Field-dependent magnetization at 2, 100 and 300 K for (a–c) CTO, (d–f) CNTO, and (g–i) NTO for pristine, 400 °C and 500 °C calcined compounds.

of the particles. However, as shown in Fig. 4(a, d and g), a linear *M–H* is due to paramagnetic behavior. A weak FM behavior at low temperatures and paramagnetic behavior at high temperatures in these nano-sized pristine compounds can be understood in terms of blocked spins (in the superparamagnetic state) overcoming the energy barrier using the thermal energy at high temperatures (NiO,[21] CuO[22] and MnO[23]). In contrast, the calcinated crystalline nanoparticles of MTO show AFM order under $H = 0$. The strong AFM coupling is evident from the linear magnetization isotherms at 2 K. Overall, a transition from superparamagnetic (pristine and non-crystalline) to AFM (calcinated and crystalline) is reported for these MTO nanoparticles.

This study particularly correlates the observed magnetic behavior with non-crystalline to crystalline structural transition as a function of particle size.[24,25] The key difference between the observed magnetic behavior is that no two atomic sites are equivalent in a non-crystalline structure, whereas many macroscopic directions may be equivalent in crystalline nanostructures. Thus, this new class of nanomaterials provides excellent control over magnetic behavior *via* particle size and crystallographic structural ordering, not recounted so far. Moreover, since applications of magnetic materials rely on the stable magnetic order, the magnetic anisotropy energy along certain directions becomes comparable to the thermal energy with the reduction in particle size, forcing nanoparticles to lose their stable magnetic order and become superparamagnetic.[26] In contrast, the current work presents a novel class of materials that display stable magnetic order in nanoparticles of size ~6 nm (Table S3, ESI†).

Conclusions

In summary, $Co_{1-x}Ni_xTeO_4$ (x = 0, 0.5, and 1) nanomaterials with different particle sizes are prepared by a sol–gel method

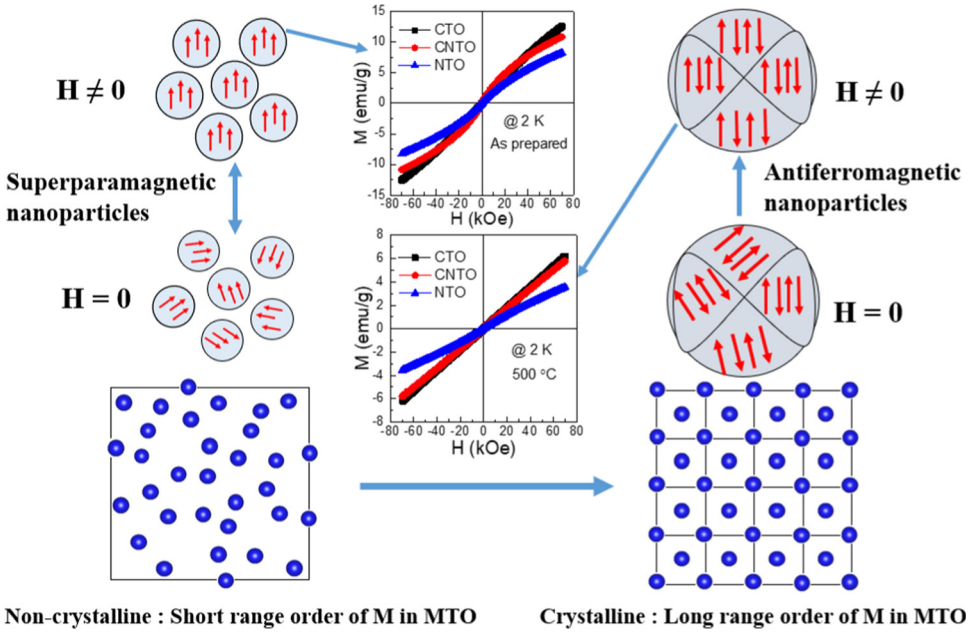

Fig. 5 *M*–*H* curves of pristine and 500 °C calcined MTO compounds along with a schematic diagram of the magnetic response with and without magnetic field and structural ordering.

and their structural and magnetic interactions are investigated. Microstructural and structural data evidence the increase in particle size and long-range structural ordering with the calcination temperature. These nanomaterials exhibit different magnetic interactions with different calcination temperatures. Calcination at lower temperatures shows the short-range non-crystalline structure and superparamagnetic behavior, while calcination at higher temperatures exhibits long-range ordering in both the crystal and magnetic structures. Noted direct correlation between structural ordering and magnetic interactions *via* temperature and field-dependent magnetization measurements presents a new family of nanomaterials with a unique structure and magnetic property control.

Conflicts of interest

The authors declare no conflicts of interest.

Acknowledgements

The authors acknowledge SAIF-IIT Bombay and NCPRE-IIT Bombay for providing experimental facilities. H. S. acknowledges the Science & Engineering Research Board, DST, India, for support under NPDF project PDF/2016/001159. E. R. and H. S. also acknowledge The Academy of Finland (grant #311934) for the financial supports.

References

1 G.-H. Lee, H. Moon, H. Kim, G. H. Lee, W. Kwon, S. Yoo, D. Myung, S. H. Yun, Z. Bao and S. K. Hahn, Multifunctional materials for implantable and wearable photonic healthcare devices, *Nat. Rev. Mater.*, 2020, **5**, 149–165.

2 S. Tong, C. A. Quinto, L. Zhang, P. Mohindra and G. Bao, Size-Dependent Heating of Magnetic Iron Oxide Nanoparticles, *ACS Nano*, 2017, **11**, 6808–6816.

3 Z. Cheng, Q. Fu, H. Duan, Z. Cui, Y. Xue and W. Zhang, Size-Dependent Thermodynamics of Structural Transition and Magnetic Properties of Nano-Fe2O3, *Ind. Eng. Chem. Res.*, 2019, **58**, 8418–8425.

4 K. Pathakoti, M. Manubolu and H. M. Hwang, Nanostructures: Current uses and future applications in food science, *J. Food Drug Anal.*, 2017, **25**, 245–253.

5 R. Dronskowski, The little maghemite story: A classic functional material, *Adv. Funct. Mater.*, 2001, **11**, 27–29.

6 Q. Zhang, P. Wang, X. Li, Y. Yang, X. Liu, F. Zhang, Y. Ling and Y. Zhou, Preparation of highly dispersed γ-Fe2O3 and GdPO4 co-functionalized mesoporous carbon spheres for dual-mode MR imaging and anti-cancer drug carrying, *J. Mater. Chem. B*, 2017, **5**, 3765–3770.

7 S. Yang, C. Liu, H. Chang, L. Ma, Z. Qu, N. Yan, C. Wang and J. Li, Improvement of the activity of γ-Fe2O3 for the selective catalytic reduction of NO with NH3 at high temperatures: NO reduction versus NH3 oxidization, *Ind. Eng. Chem. Res.*, 2013, **52**, 5601–5610.

8 N. M. Li, K. M. Li, S. Wang, K. Q. Yang, L. J. Zhang, Q. Chen and W. M. Zhang, Gold embedded maghemite hybrid nanowires and their gas sensing properties, *ACS Appl. Mater. Interfaces*, 2015, **7**, 10534–10540.

9 V. G. De Paula, L. M. Da Silva, A. O. Dos Santos, R. Lang, L. Otubo, A. A. Coelho and L. P. Cardoso, Magnetocaloric effect and evidence of superparamagnetism in GdA l2 nanocrystallites: A magnetic-structural correlation, *Phys. Rev. B*, 2016, **93**, 1–9.

10 S. D. Tiwari and K. P. Rajeev, Paramagnetic to ferromagnetic transition and superparamagnetic blocking in Ni (OH) 2 nanoparticles, *Phys. Rev. B: Condens. Matter Mater. Phys.*, 2008, **77**, 6–11.

11 R. Caciuffo, D. Rinaldi, G. Barucca, J. Mira, J. Rivas, M. A. Señarís-Rodríguez, P. G. Radaelli, D. Fiorani and J. B. Goodenough, Structural details and magnetic order of La1-*x*Sr*x*CoO3 ($x \leq 0.3$), *Phys. Rev. B: Condens. Matter Mater. Phys.*, 1999, **59**, 1068–1078.

12 W. Xia, H. Wu, P. Xue and X. Zhu, Microstructural, Magnetic, and Optical Properties of Pr-Doped Perovskite Synthesized via Sol-Gel Process, *Nanoscale Res. Lett.*, 2018, **13**, 135.

13 T. Zhang, X. P. Wang, Q. F. Fang and X. G. Li, Magnetic and charge ordering in nanosized manganites, *Appl. Phys. Rev.*, 2014, **1**, 031302.

14 A. K. Patel, M. R. Panda, E. Rani, H. Singh, S. S. Samatham, A. Nagendra, S. N. Jha, D. Bhattacharyya, K. G. Suresh and S. Mitra, Unique Structure-Induced Magnetic and Electrochemical Activity in Nanostructured Transition Metal Tellurates Co_{1-x} Ni_x TeO_4 (x = 0, 0.5, and 1), *ACS Appl. Energy Mater.*, 2020, **3**, 9436–9448.

15 M. R. Panda, A. Raj K, A. Ghosh, A. Kumar, D. Muthuraj, S. Sau, W. Yu, Y. Zhang, A. K. Sinha, M. Weyland, Q. Bao and S. Mitra, Blocks of molybdenum ditelluride: A high rate anode for sodium-ion battery and full cell prototype study, *Nano Energy*, 2019, **64**, 103951.

16 B. R. Dahal, R. P. Dulal, I. L. Pegg and J. Philip, Electrical transport and magnetic properties of cobalt telluride nanostructures, *J. Vac. Sci. Technol., B: Nanotechnol. Microelectron.: Mater., Process., Meas., Phenom.*, 2016, **34**, 051801.

17 C. R. Feger, G. L. Schimek and J. W. Kolis, Hydrothermal Synthesis and Characterization of $M_2Te_3O_8$ (M = Mn, Co, Ni, Cu, Zn): A Series of Compounds with the Spiroffite Structure, *J. Solid State Chem.*, 1999, **143**, 246–253.

18 H. Singh, H. Ghosh, T. V. Chandrasekhar Rao, G. Sharma, J. Saha and S. Patnaik, Short range ferromagnetic, magnetoelectric, and magneto-dielectric effect in ceramic Co_3 TeO_6, *J. Appl. Phys.*, 2016, **119**, 044104.

19 H. Singh, H. Ghosh, C. L. Prajapat and M. R. Singh, Griffiths like robust ferromagnetism in Co_{3-x} Mn_x TeO_6; (x = 0.5, 1, 2), *Mater. Res. Bull.*, 2016, **80**, 273–279.

20 S.-C. Zhu, G.-W. Chen, D. Zhang, L. Xu, Z.-P. Liu, H. Mao and Q. Hu, Topological Ordering of Memory Glass on Extended Length Scales, *J. Am. Chem. Soc.*, 2022, **144**, 7414–7421.

21 T. Iimori, Y. Imamoto, N. Uchida, Y. Kikuchi, K. Honda, T. Iwahashi and Y. Ouchi, Magnetic moment distribution in nanosized antiferromagnetic NiO, *J. Appl. Phys.*, 2020, **127**, 023902.

22 T. Sorop, Superparamagnetic behaviour of antiferromagnetic DyPO4 nanoparticles, *J. Magn. Magn. Mater.*, 2004, **272–276**, 1573–1574.

23 S. Sako, Y. Umemura, K. Ohshima, M. Sakai and S. Bandow, Magnetic Property of Antiferromagnetic MnO Ultrafine-Particle, *J. Phys. Soc. Jpn.*, 1996, **65**, 280–284.

24 Q. Li, C. W. Kartikowati, S. Horie, T. Ogi, T. Iwaki and K. Okuyama, Correlation between particle size/domain structure and magnetic properties of highly crystalline Fe3O4 nanoparticles, *Sci. Rep.*, 2017, **7**, 9894.

25 N. V. Rama Rao, R. Gopalan, M. Manivel Raja, V. Chandrasekaran and K. G. Suresh, Mössbauer studies on structural ordering and magnetic properties of melt-spun Ni–Fe–Ga ribbons, *Appl. Phys. Lett.*, 2008, **93** 202503.

26 V. Skumryev, S. Stoyanov, Y. Zhang, G. Hadjipanayis, D. Givord and J. Nogués, Beating the superparamagnetic limit with exchange bias, *Nature*, 2003, **423**, 850–853.

